Optik - International Journal for Light and Electron Optics 199 (2019) 163337

Contents lists available at ScienceDirect

Optik

journal homepage: www.elsevier.com/locate/ijleo

Original research article

# Adaptive super-twisting sliding mode control for stabilization platform of laser seeker based on extended state observer

Mingyue Zhang[a], Yongliang Guan[b,*], Weiwei Zhao[a]

[a] Changchun Institute of Optics, Fine Mechanics and Physics, Chinese Academy of Sciences, No. 3888, Dongnanhu Rd., Changchun 130033, China
[b] Chang Guang Satellite Technology Co., LTD, Changchun, 130033, China

ARTICLE INFO

*Keywords:*
Seeker
Stabilization platform of the seeker
Super-twisting sliding mode control
Extended state observer

ABSTRACT

In this paper, the stabilization platform of the seeker is analyzed to stabilize the photo-electric device by isolating the disturbances caused by vibration and turbulence from external conditions, as well as mechanical coupled torque, coiling, unbalanced torque and plant parameter uncertainty due to inner conditions. There are two important indexes to describe the performance of disturbance isolation, and these are the coupling coefficient and disturbance rejection rate. In order to improve the disturbance isolation performance of the stabilization platform of the seeker, an adaptive super-twisting sliding mode controller with an extended state observer is proposed. The adaptive super-twisting sliding mode control strategy is designed to achieve stabilized control of the stabilization platform of the seeker. The extended state observer is used to estimate and compensate for disturbances and model uncertainties. The stability analysis of the control strategy is discussed using Lyapunov stability theory. Simulation and experimental results are also presented to illustrate the effectiveness of the proposed control strategy. The proposed controller provides a better level of disturbance rejection compared to the conventional PI-DOB controller.

## 1. Introduction

Two-axis gimbal stabilization platforms are widely adopted to hold the line of sight (LOS) stationary or point the LOS of radar, laser, infrared and visual camera payloads to distant objects. The seeker stabilization platform is used to stabilize the photo-electric device by isolating the disturbances caused by external vibration and turbulence from internal mechanical coupled torque, coiling, unbalanced torque and plant parameter uncertainty. As a result, the seeker stabilization platform is highly non-linear. A very important index of the stabilization platform is the disturbance rejection rate, and there are two methods to improve it. One is to use high performance sensors and improve the mechanical rigidity, which increases the weight and cost of the system. The other one is to design an appropriate control strategy to achieve precision and stable performance.

Taking into account the above-mentioned characteristics, over the past decade substantial effort has been made in exploring the utility of compound controllers to improve the performance of the stabilization platform. Generally, there are three loops to control the stabilization platform. The current loop (inner loop) aims to reduce the influence of motor EMF (back electromotive force), variations of the stator resistance and to provide a high bandwidth for the stabilization loop. The stabilization loop (middle loop) is utilized to reject the vast majority of disturbances of the missile's motion on the sensor [1]. The tracking loop (outer loop) is utilized to ensure the LOS pointing toward the target. A general method for controlling the system is using a proportional integral derivative

* Corresponding author.
*E-mail addresses:* zyy_2011@163.com (M. Zhang), zyyqn@foxmail.com (Y. Guan), zhaowei5512@foxmail.com (W. Zhao).

https://doi.org/10.1016/j.ijleo.2019.163337
Received 4 June 2019; Accepted 29 August 2019

(PID) controller. In addition, some advanced control strategies, such as fuzzy PID controllers [2], a two-degree of freedom internal model controllers [3], high-order sliding mode control approaches [4], and H∞ controllers [5] have been also proposed to solve the stabilization problem of the stabilization platform. However, they are complex and the parameters of the controller are hard to tune. In addition, the controller cannot provide satisfactory performance under serious disturbances.

Sliding mode control (SMC) has well-known merits of precision and robustness against disturbance and uncertainties [6]. However, the main disadvantage of classical SMC is chattering, and there are two methods to alleviate this problem. The first method is to replace the sign function by a high-slope saturation function [7]. However, although chattering can be reduced through this method, an indefinite steady-state error will occur depending on the selection of the boundary layer thickness [8,9]. The second method is to adopt higher order sliding mode control techniques, which avoids the drawbacks of traditional SMC while retaining its advantages. Second-order sliding mode control (SOSMC) is a commonly used method to attenuate the chattering problem, but it is difficult to acquire the high-order time derivatives of the sliding variables.

The super twisting (STW) algorithm, proposed by Levant [10], is always used to design SOSMC [11], and the compound controller only requires knowledge of the sliding variable, but not its time derivatives [12]. However, the controller also requires knowledge of the boundaries of the seeker's disturbances and their gradient. In many cases, this boundary is hard to determine. It is worth noting that an adaptive controller can adapt the gain magnitude with respect to the disturbance of the system. The adaptive-gain STW (ASTW) control law, which handles perturbed plant dynamics with disturbances / uncertainties of a certain class with unknown boundaries, was proposed by Shtessel et al. [13], and can attenuate the chattering phenomenon.

It is well known that the estimation of uncertainty and disturbance is crucial for seeker stabilization platforms, and observer-based controller design is one of the most popular methods in the field of motion control [14,15]. Thus, extended state observer (ESO) and disturbance observer (DOB) are widely used to estimate the disturbance. The ESO based on Active Disturbance Rejection Controller (ADRC) [16] has been used in many applications [17]. Since nonlinear ESO has many parameters to adjust, the linear ESO is commonly preferred. Traditional PI-DOB control strategy [18] depends on the PI gain and disturbance estimation, but if the result of the observer is not accurate, such method will be ineffective. In addition, it requires more sensors than ESO to guarantee the accuracy of the DOB. That is to say, the ESO requires the minimum information of the system to estimate both the disturbance and the system state [19].

Motivated by above methods, in order to improve the performance of the platform, a composite control method based on an adaptive super-twisting controller scheme and a linear second-order ESO is proposed to achieve the platform speed tracking of the reference signal. Rigorous stability analysis is applied using the Lyapunov method to show the global stability of the complete closed-loop system. The main contribution of this paper is to propose an efficient controller, which has a continuous control input and strong robustness against parameter perturbations and external disturbances.

The rest of this paper is organized as follows. A dynamical model of the stabilization platform is presented in Section 2. In Section 3, the problem is formulated and the controller design is introduced. Section 4 describes the simulation analysis, and the proposed control strategy is compared with other controllers. Section 5 shows the experiments of the system to illustrate feasibility of practical use of the proposed control strategy. Finally, Section 6 gives a brief summary of the paper and the conclusion.

## 2. System description and mathematical model

### 2.1. General system descriptions

As is shown in Fig. 1, the stabilization platform of the seeker consists of an optics system, an inner gimbal (elevation), an outer gimbal (azimuth), potentiometers, a rate gyro, and torque motors. When the missile rotates or jitters due to wind disturbances and vibrations, the stabilization platform of the seeker provides rejection of disturbances and controls the LOS of the optics system.

Three coordinate frames are used to define the gimbal motion. As shown in Fig. 1, O-x0y0z0 is the reference coordinate frame of

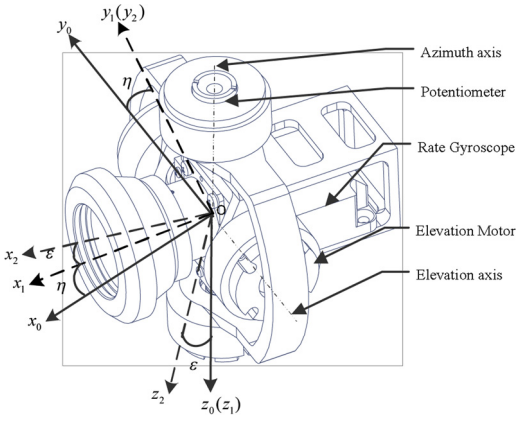


**Fig. 1.** Gimbaled seeker schematic.

the missile, O-x1y1z1 is the coordinate frame of the yaw gimbal, while O-x2y2z2 is the coordinate frame of the pitch gimbal. The latter houses an rate sensor (Micro Electronic Mechanical System(MEMS) gyro), which supplies directly the angular velocity of the two gimbals with respect to the inertial frame. $\theta_a$ and $\theta_e$ are the azimuth and elevation angle respectively. Potentiometers are used to measure the angular position of the two gimbals for the seeker's search mode. Two DC torque motors are used to provide torque to the gimbals. All the coordinate frames are defined using the right-handed rule and have the same origin for simplicity. The coordinate set is used to formulate Newton-Euler equations of the two gimbals. The stabilization loop consists of the rate gyro, the torque motor, the controller and the gimbals.

### 2.2. Gimbal kinematic relationships

The coordinate transformation matrix between the missile's coordinate system and the outer coordinates' frame is:

$$\mathbf{R}_{0,1}(\theta_a) = \begin{bmatrix} \cos\theta_a & \sin\theta_a & 0 \\ -\sin\theta_a & \cos\theta_a & 0 \\ 0 & 0 & 1 \end{bmatrix} \tag{1}$$

The transformation matrix between the outer coordinates' frame and the inner coordinates' frame is:

$$\mathbf{R}_{1,2}(\theta_e) = \begin{bmatrix} \cos\theta_e & 0 & -\sin\theta_e \\ 0 & 1 & 0 \\ \sin\theta_e & 0 & \cos\theta_e \end{bmatrix} \tag{2}$$

In this paper, bold symbols signify vector variables. The angular velocity of the base is $\boldsymbol{\omega}_0 = [\omega_{0x} \quad \omega_{0y} \quad \omega_{0z}]^T \in \Re^{3\times 1}$. Based on the transformation matrix, the angular velocity $\boldsymbol{\omega}_1$ between the outer gimbal and base, and the angular velocity $\boldsymbol{\omega}_2$ between the inner gimbal and outer gimbal are as follows:

$$\begin{cases} \boldsymbol{\omega}_1 = \mathbf{R}_{0,1}(\theta_a)\boldsymbol{\omega}_0 + \mathbf{w}_1\dot{\theta}_a \\ \boldsymbol{\omega}_2 = \mathbf{R}_{1,2}(\theta_e)\boldsymbol{\omega}_1 + \mathbf{w}_2\dot{\theta}_e \end{cases} \tag{3}$$

where $\boldsymbol{\omega}_1 = [\omega_{1x} \quad \omega_{1y} \quad \omega_{1z}]^T$, $\mathbf{w}_1 = [0 \quad 1 \quad 0]^T$, $\boldsymbol{\omega}_2 = [\omega_{2x} \quad \omega_{2y} \quad \omega_{2z}]^T$, $\mathbf{w}_2 = [0 \quad 0 \quad 1]^T$.

The angular velocity $\boldsymbol{\omega}_2$ between the inner gimbal, outer gimbal and base is:

$$\boldsymbol{\omega}_2 = \mathbf{R}_{1,2}(\theta_e)\mathbf{R}_{0,1}(\theta_a)\boldsymbol{\omega}_0 + \mathbf{R}_{1,2}(\theta_e)\mathbf{w_1}\dot{\theta}_a + \mathbf{w}_2\dot{\theta}_e \tag{4}$$

By differentiating $\boldsymbol{\omega}_2$, we can write Eq. (4) in the form:

$$\dot{\boldsymbol{\omega}}_2 = \mathbf{R}_{1,2}(\theta_e)\dot{\boldsymbol{\omega}}_1 + \mathbf{Q}_{1,2}(\theta_e)\boldsymbol{\omega}_1\dot{\theta}_e + \mathbf{w}_2\ddot{\theta}_e \tag{5}$$

where $\mathbf{Q}_{1,2}(\theta_e) = \begin{bmatrix} -\sin\theta_e & 0 & -\cos\theta_e \\ 0 & 0 & 0 \\ \cos\theta_e & 0 & -\sin\theta_e \end{bmatrix}$.

### 2.3. Gimbal dynamics model

Based on rigid body dynamics and the Newton-Euler equation [20], the expression for the elevation axis' angular momentum theorem can be derived as:

$$\mathbf{J}_I\dot{\boldsymbol{\omega}}_2 + (\boldsymbol{\omega}_2 \times \mathbf{J}_I\boldsymbol{\omega}_2) = \mathbf{L}_I \tag{6}$$

where $\mathbf{J}_I = diag(J_{Ix} \quad J_{Iy} \quad J_{Iz})$ is the inertia tensor of the inner gimbal, $\mathbf{L}_I$ is the resultant moment, and the product of inertia is omitted for the two gimbals. $\mathbf{L}_I$ can be derived as:

$$\mathbf{L}_I = \begin{bmatrix} T_{Ix} - T_{Iux} \\ T_{Iy} - T_{Iuy} - T_{If\omega} \\ T_{Iz} - T_{Iuz} \end{bmatrix} \tag{7}$$

where $T_{Ix}$, $T_{Iz}$ are the reaction torques between inner gimbal and outer gimbal, $T_{Iy}$ is the control torque of motor, $T_{If\omega}$ is the sum of the friction and cable restraint torque, and $T_{Iux}$, $T_{Iuy}$, $T_{Iuz}$ are the unbalance torques of the inner gimbal.

**Assumption 1.** The gimbals' rotational axes are aligned with the principal axes of inertia. As a result, the inertia matrix is assumed to be diagonal for the two gimbals.

The elevation control axis is the inner gimbal's $y$ axis. Therefore, by expanding the expression of Eq. (6) the dynamics equation is given as:

$$J_{Iy}\dot{\omega}_{2y} = T_{Iy} - T_{Iuy} - \omega_{2z}\omega_{2x}(J_{Ix} - J_{Iz}) - [(K_{If}\dot{\theta}_e + K_{I\omega}\theta_e) + (T_{I,fric} + T_{I,CR})] \tag{8}$$

where subscript y denotes that the elevation control axis is the y-axis. The friction torque is divided into the linear friction torque $K_{If}\dot{\theta}_e$ and the non-linear friction $T_{I,fric}$, and the cable restraint torque is divided into the linear restraint torque $K_{1\omega}\theta_e$ and nonlinear cable restraint $T_{I,CR}$.

As the stabilized loop adopts the direct LOS stabilization with the angular rate gyro mounted on the LOS axis(elevation axis), it is necessary to modify the kinematic torque of the inner gimbal to an expression consisting of $\omega_{2y}$, $\omega_{2z}$, $\theta_e$, $\theta_a$, and the missile disturbance $\boldsymbol{\omega}_0$. Substituting Eq. (3) into Eq. (8), the dynamics equations are given as:

$$J_{Iy}\dot{\omega}_{2y} = T_{Iy} + T_{IDbase} - T_{Iuy} - T_{I,fric} - T_{I,CR} - K_{If}\omega_{2y} + K_{I\omega}\int_0^t \omega_{2y}(\tau)d\tau - \omega_{2z}\left(\frac{\omega_{1x} - \sin\theta_e\omega_{2z}}{\cos\theta_e}\right)(J_{Ix} - J_{Iz}) \tag{9}$$

where $T_{IDbase} = K_I f(cos\theta_a\omega_{0y} - sin\theta_a\omega_{0x}) + K_I\omega\int_0^t (cos\theta_a(\tau)\omega_{0y}(\tau) - sin\theta_a(\tau)\omega_{0x}(\tau))d\tau$,and it is the base disturbance for the inner gimbal.

The expression for the azimuth axis angular momentum theorem can be derived as:

$$\mathbf{J}_O\dot{\boldsymbol{\omega}}_1 + (\boldsymbol{\omega}_1 \times \mathbf{J}_O\boldsymbol{\omega}_1) + \mathbf{L}_{O,I} = \mathbf{L}_O \tag{10}$$

where $\mathbf{J}_O = diag(J_{Ox}\ \ J_{Oy}\ \ J_{Oz})$ is the inertia tensor of the outer gimbal, $\mathbf{L}_O$ is the resultant moment and can be derived as:

$$\mathbf{L}_O = \begin{bmatrix} T_{Ox} - T_{Oux} \\ T_{Oy} - T_{Ouy} \\ T_{Oz} - T_{Ouz} - T_{Of\omega} \end{bmatrix} \tag{11}$$

where $\mathbf{L}_{O,I} = \mathbf{R}_{1,2}(\theta_e)[\mathbf{J}_I\dot{\boldsymbol{\omega}}_2 + (\boldsymbol{\omega}_2 \times \mathbf{J}_I\boldsymbol{\omega}_2)]$, $T_{Ox}$, $T_{Oy}$ are the reaction torques between the outer gimbal and the base, $T_{Oz}$ is the control torque of the motor, $T_{Of\omega}$ is the sum of the friction and cable restraint torque, and $T_{Oux}$, $T_{Ouy}$, $T_{Ouz}$ are the unbalance torques of the outer gimbal.

Because the angular rate gyro is mounted on the inner gimbal, the azimuth control axis is the inner gimbal's $z$ axis. However, the azimuth axis' dynamics are generated by the third element of Eq. (10). Substituting Eq. (5) into Eq. (10), expanding the cross product terms and substituting the kinematic torques leads to:

$$\begin{aligned} J_s\dot{\omega}_{2z} = {} & \sin\theta_e(J_{Oz} + J_{Ix})\dot{\omega}_{1x} + (J_{Oz}\omega_{2x} - J_{Ix}\omega_{1z}\sin\theta_e)\dot{\theta}_e - \cos\theta_e[\omega_{1x}\omega_{1y}(J_{Oy} - J_{Ox}) - \omega_{2y}\omega_{2z}J_{Iz}\sin\theta_e + \omega_{2y}\omega_{1x}J_{Iy} - \omega_{2x}\omega_{2y}J_{Ix}\cos\theta_e] \\ & + \cos\theta_e[T_{Oz} - T_{Ouz} - T_{O,fric} - T_{O,CR}] - \cos\theta_e K_{Of}\dot{\theta}_a - \cos\theta_e K_{O\omega}\theta_a \end{aligned} \tag{12}$$

where subscript $z$ denotes that the elevation control axis is the $z$ axis. The friction torque is divided into the linear friction torque $K_{Of}\dot{\theta}_a$ and nonlinear friction $T_{O,fric}$, and cable restraint torque is divided into linear restraint torque $K_{O\omega}\theta_a$ and non-linear cable restraint $T_{O,CR}$. $J_s$ is as follows:

$$J_s = J_{Oz} + J_{Iz}\cos^2\theta_e + J_{Ix}\sin^2\theta_e \tag{13}$$

As the stabilized loop adopts the direct LOS stabilization with the angular rate gyro mounted on the LOS axis, it is necessary to modify the kinematic torque of the outer gimbal to the expression consisting of $\omega_{2y}$, $\omega_{2z}$, $\theta_e$, $\theta_a$, and the missile disturbance $\boldsymbol{\omega}_0$. $\omega_{2x}$ and $\omega_{1z}$ can be described as :

$$\omega_{2x} = \frac{1}{\cos\theta_e}(\omega_{1x} - \omega_{2z}\sin\theta_e),\ \omega_{1z} = \frac{1}{\cos\theta_e}(\omega_{2z} - \omega_{1x}\sin\theta_e) \tag{14}$$

The main nonlinear factor comes from base oscillations, model uncertainty, variable load and friction and cable torque. Substituting Eq. (14) into Eq. (12), the torque is as follows:

$$J_s\dot{\omega}_{2z} = T_{ODbase} + \cos\theta_e[T_{Oz} - T_{Ouz} - T_{O,fric} - T_{O,CR}] - K_{Of}\omega_{2z} - g_y\omega_{2y}\omega_{1x} - g_{yz}\omega_{2y}\omega_{2z} - \cos\theta_e K_{O\omega}\int_0^t \frac{1}{\cos\theta_e(\tau)}\omega_{2z}(\tau)d\tau$$

$$\begin{aligned} T_{ODbase} = {} & \sin\theta_e(\dot{\omega}_{0x}\cos\theta_a + \dot{\omega}_{0y}\sin\theta_a - \omega_{1y}\omega_{1x}\tan\theta_e - \omega_{1y}\omega_{0z})(J_{Oz} + J_{Ix}) + K_{Of}(\sin\theta_e\omega_{1x} + \cos\theta_e\omega_{0z}) \\ & - [\frac{1}{\cos\theta_e}(J_{Oz} + \sin^2\theta_e J_{Ix}) + \cos\theta_e(J_{Oy} - J_{Ox})]\omega_{1x}\omega_{1y} + \cos\theta_e K_{O\omega}\int_0^t (\omega_{1x}(\tau)\tan\theta_e(\tau) + \omega_{0z}(\tau))d\tau \end{aligned} \tag{15}$$

where $g_y = \cos\theta_e(J_{Iy} - J_{Ix}) - \frac{1}{\cos\theta_e}(J_{Oz} + \sin^2\theta_e J_{Ix})$, $g_{yz} = (J_{Iz} + J_{Ix})\tan\theta_e - \cos\theta_e\sin\theta_e(J_{Iz} - J_{Ix})$, $T_{ODbase}$ is the base disturbance for the outer gimbal.

Let $x_1 = \int_0^t \omega_{2y}(\tau)d\tau$, $x_2 = \dot{x}_1 = \omega_{2y}$, $x_3 = \int_0^t \omega_{2z}(\tau)d\tau$, $x_4 = \dot{x}_3 = \omega_{2z}$. Then, Eq. (10) and Eq. (15) can be described by the state variables $x_1$, $x_2$, $x_3$, $x_4$. The coupled state-space form for the platform can then be expressed in the following condensed equation:

$$\dot{\mathbf{x}} = \mathbf{A}\mathbf{x} + \mathbf{F} + \mathbf{J}^{-1}[T_m + T_d] \tag{16}$$

where $\mathbf{F}^T = [0,\ \frac{J_{Ix} - J_{Iz}}{J_{Iy}}\omega_{2z}^2\tan\theta_a,\ 0,\ \frac{g_{yz}\omega_{2y}\omega_{2z}}{J_s}]$ $T_{Id} = -T_{Iuy} - T_{I,fric} - T_{I,CR} + T_{IDbase}$, $T_{Od} = -T_{Ouy} - T_{O,fric} - T_{O,CR} + T_{ODbase}$,

$\mathbf{T}_m^T = [0,\ T_{Iy},\ 0,\ T_{Oz}]$, $\mathbf{T}_d^T = [0,\ T_{Id},\ 0,\ T_{Od}]$, $\mathbf{J}^{-1} = \begin{bmatrix} 0 & 0 & 0 & 0 \\ 0 & J_{Iy}^{-1} & 0 & 0 \\ 0 & 0 & 0 & 0 \\ 0 & 0 & 0 & J_s^{-1} \end{bmatrix}$, $\mathbf{A} = \begin{bmatrix} 0 & 1 & 0 & 0 \\ \frac{-K_{I\omega}}{J_{Iy}} & \frac{-K_{If}}{J_{Iy}} & 0 & \frac{J_{Ix} - J_{Iz}}{J_{Iy}}\omega_{1x} \\ 0 & 0 & 0 & 1 \\ 0 & \frac{g_y\omega_{1x}}{J_s} & \frac{-K_{O\omega}}{J_s} & \frac{-K_{Of}}{J_s} \end{bmatrix}$

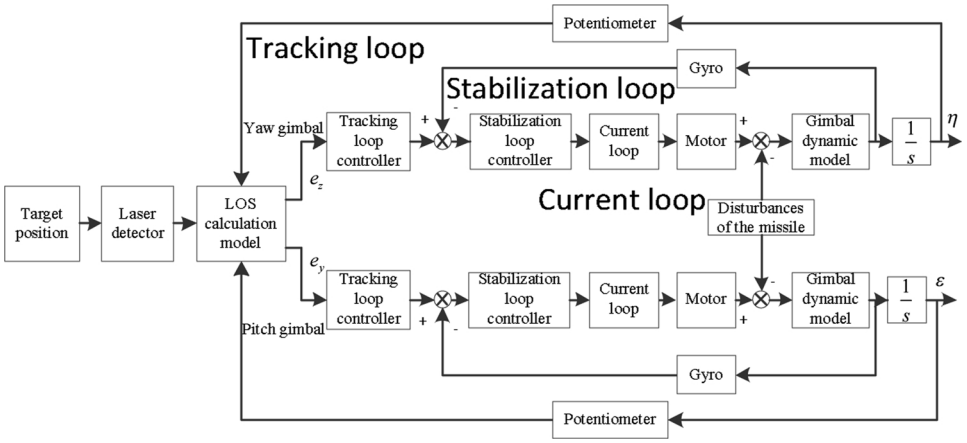


**Fig. 2.** Block diagram of three loop control system structure of the stabilization platform.

### 2.4. Stablizing principle of LOS

Based on the above kinematic and dynamic equations, the stabilized condition should obey the following equation.

$$\begin{cases} \omega_{1y} = \omega_{0y} + \dot{\theta}_e = 0 \\ \omega_{2z} = \omega_{1z} + \dot{\theta}_a = 0 \end{cases} \tag{17}$$

This paper presents a three closed-loop control strategy for the dynamical model, which is widely used in the control of inertial stabilization platforms. The classical three-loop control block diagram is depicted in Fig. 2. When the optical axis of the guidance system deviates from the position of the target, the laser detector detects the angular position error signal of the target. Then, the platform is driven to rotate so that the optical axis can track the target. $e_y$ and $e_z$ are the internal and external frame angular position errors respectively of the target, processed by the seeker detector. The internal and external frame angular position error signals need to be eliminated by the tracking loop. And the input signals of the velocity loop are obtained by the control output of the tracking loop. Then, the input of the current loop is obtained by the stabilization loop. The output of the current loop drives the motor and rotation mechanism. In the current loop, a complete H-bridge MOSFET Brushed Motor Control System in an electrically isolated hermetic package is used. We set the parameters of the driver so that the -3 dB bandwidth of the current loop is over 1000 Hz. The difference between the inner gimbal and outer gimbal is that the outer gimbal control needs the secant gain function compensation of the elevation angle. Here, without loss of generality, we consider the inner gimbal for the design of the ESO and ASTW controllers.

The dynamic model of the direct drive DC torque motor considered in this paper can be described using [21]:

$$\begin{cases} \dfrac{di}{dt} = \dfrac{1}{L}(Ri + U - K_m\dfrac{d\theta}{dt}) \\ \dfrac{d\omega}{dt} = \dfrac{1}{J_{GES}}(K_t i - B\dfrac{d\theta}{dt} - T_L) \end{cases} \tag{18}$$

where $i$ is the motor armature current, $L$ is the armature inductance, $R$ is armature resistance, $U$ is the input voltage, $K_m$ is the back electromotive force constant, $\theta$ is the angular position, $J_{GES}$ is the equivalent moment of inertia of the motor and load, $K_t$ is the coefficient of electromechanical torque, $B$ is the mechanical dumping constant, and $T_L$ is the load torque.

## 3. Problem formulation and eso-based controller design

The stabilization problem is to attenuate persistent disturbances of the system. The goal is to design a compound control strategy to make the system robustly stabilized in finite-time. The control strategy is shown in Fig. 3, which consists of an ESO and an ASTW sliding mode controller. We describe the ASTW – ESO controller briefly.

### 3.1. ESO design

The design of the extended state observer is as follows. Taking the stabilization loop of the elevation axis as an example, the state space equation of the elevation gimbal after the current closed loop can be expressed as follows [22]:

$$\begin{cases} \dot{x} = b_0 u + d \\ y = x \end{cases} \tag{19}$$

The system is a single input first order system, where $x$ is the state, $y = x = \omega$ is the system output, $u$ is control input, $b_0$ is the

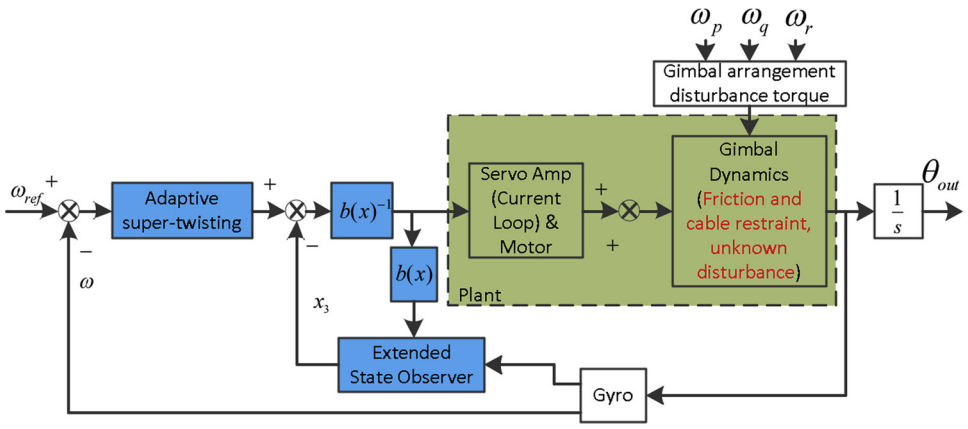


**Fig. 3.** Control block diagram of the proposed controller.

constant $b_0 = \frac{1}{J_{GES}}$, $d$ is the lumped unknown dynamics disturbance and includes the supporter disturbance, the balanced torque and friction torque.

**Assumption 2.** The functions $d$ and $\dot{d}$ are bounded over the domain of interest. Their initial value is zero, while their boundaries are not known.

The ESO aims to estimate the unknown disturbance $d$ [23]. According to the ESO design method, a second-order ESO is introduced as follows:

$$\begin{cases} e = z_1 - \omega \\ \dot{z}_1 = z_2 - \beta_1 e + b_0 u \\ \dot{z}_2 = -\beta_2 e \\ \hat{d} = z_2 \end{cases} \tag{20}$$

where $\omega$ is the velocity of the system, $\beta_1$, $\beta_2$ are the observer gains, $z_1$, $z_2$ are the outputs of the ESO, with $z_1$ being the estimate of the state variable $x$, and $z_2$ being the estimate of the total disturbance $d$. The method of bandwidth-parameterization is applied to the ESO design [23], thus $\beta_1 = 2\omega_0$, $\beta_2 = \omega_0^2$. The ESO has only one parameter to be tuned, which is $\omega_0$.

The main objective is to estimate the total disturbance in real time. However, the high bandwidth of the parameters of the ESO [24] improves the response, but will magnify sensor noise and dynamic uncertainties. Therefore, a trade-off between noise and rapidity must be made empirically. The convergence of this observer is shown in [25].

After the compensation of the ESO, Eq. (19) can be written as follows:

$$\dot{x} = \dot{\omega} = b_0 u + d - \hat{d} = b_0 u + \tilde{d} \tag{21}$$

The approximate value of the disturbance is $\hat{d}$, while the approximation error is defined as $\tilde{d} = d - \hat{d}$.

### 3.2. Adaptive super twisting sliding mode controller design

The sliding surface is defined as follows [26]:

$$s = \omega_d - \omega \tag{22}$$

where $\omega_d$ represents the desired speed. The stabilizing control problem is to drive $\omega$ to the desired $\omega_d$.

The objective of the controller is to make sure that s and $\dot{s}$ are asymptotically stable near zero. Because of imperfections in the switching devices and delays, the sliding mode control suffers from chattering. Chattering results in low control accuracy, high heat losses in electrical power circuits and high wear of moving mechanical parts. It may also excite unmodeled high-frequency dynamics, which degrades the performance of the system and may even lead to instability [7]. Utilizing the STW, the control law yields [10]:

$$\begin{cases} u_{ST} = -\alpha\ |s|^{\frac{1}{2}} sign(s) + v,\ \alpha > 0 \\ \quad\ \dot{v} = -\beta sign(s),\ \beta > 0 \end{cases} \tag{23}$$

where $\alpha$ and $\beta$ are the control gains. The system converges in finite time and has excellent robustness. The gains in standard STW implementations are affected by the disturbance boundary, which makes it difficult to compensate for the uncertainty of the system, so the adaptive STW was introduced [9], allowing the automatic determination of the gains. The adaptive gains of ASTW control are:

$$\begin{cases} \dot{\alpha} = \begin{cases} \omega_1 \sqrt{\frac{\gamma_1}{2}} sign(|s| - \mu), & \alpha > \alpha_m \\ \eta, & \alpha \le \alpha_m \end{cases} \\ \beta = 2\varepsilon\alpha \end{cases} \tag{24}$$

where $\varepsilon, \gamma_1, \omega_1, \eta, \mu, \alpha_m$ are arbitrary positive constants. The second order sliding mode controller is derived by forcing state $x$ to $\omega_d$. It can provide continuous control using only the information on $s$ and evaluation of the sign of $\dot{s}$ is not necessary.

Finite time convergence and robustness for the STW algorithms have been proved by geometrical methods [27]. Besides, it has also been proved by means of the homogeneity properties of the algorithm [28]. From Eqs. (20) and (22), the control law can be concluded as:

$$u = \frac{1}{b_0} u_{ST} = \frac{-\alpha\ |s|^{\frac{1}{2}} sign(s) + \int (-\beta sign(s))}{b_0} \tag{25}$$

The problem is to drive the sliding variable $s$ and its derivative $\dot{s}$ to zero in finite time in the presence of the bounded perturbation using continuous control. The proof of the infinite time convergence of the super twisting algorithm is given in [9]. It can guarantee reaching of the trajectories on to the sliding manifold $s = 0, \dot{s} = 0$ in finite time. Then, the system will be stable and ideally invariant to uncertainties and external disturbances.

### 3.3. Stability analysis of closed-loop dynamics

In the following, the Lyapunov function is applied on the compound controller to study the stability of the closed loop system. Another advantage of the use of Lyapunov function is that it makes it possible to obtain the relationship of the design parameters. In stability analysis, the nonlinear disturbances and coupling moments of the system are treated as disturbances, and the sufficient conditions for uniformly asymptotic stability of the system are given. Differentiating the sliding surface $s$ in Eq. (21), and substituting Eq. (21) into $\dot{s}$, the stability analysis of the system in closed-loop dynamics is described as follows:

$$\dot{s} = \dot{\omega}_d - (b_0 u + \tilde{d}) = a(x, t) + u_{ST} - \tilde{d} \tag{26}$$

where $a(x, t) = \dot{\omega}_d$.

**Assumption 3.** The parameter $\tilde{d}$ is bounded as follows:

$$|\tilde{d}| \le \rho\ |s|^{\frac{1}{2}}, \rho > 0 \tag{27}$$

where $\rho$ has finite but unknown boundaries.

Since $\dot{\omega}_d$ can be compensation in advance, Eq. (26) can be rewritten as:

$$\begin{cases} \dot{s} = -\alpha\ |s|^{\frac{1}{2}} sign(s) + v - \tilde{d} \\ \dot{v} = \int (-\beta sign(s)) \end{cases} \tag{28}$$

A new state vector is introduced as follows:

$$\chi = \left[ |s|^{\frac{1}{2}} sign(s) \quad v \right] \tag{29}$$

and the system can be rewritten as :

$$\begin{bmatrix} \dot{\chi}_1 \\ \dot{\chi}_2 \end{bmatrix} = \frac{1}{2\ |\chi_1|} \begin{bmatrix} -\alpha & 1 \\ -\beta & 0 \end{bmatrix} \begin{bmatrix} \chi_1 \\ \chi_2 \end{bmatrix} - \frac{1}{2\ |\chi_1|} \begin{bmatrix} \tilde{d} \\ 0 \end{bmatrix} \tag{30}$$

Due to assumption 3, Eq. (30) can be rewritten as:

$$\begin{bmatrix} \dot{\chi}_1 \\ \dot{\chi}_2 \end{bmatrix} = -\frac{1}{2\ |s|^{1/2}} \begin{bmatrix} \alpha - \rho & 1 \\ \beta & 0 \end{bmatrix} \begin{bmatrix} \chi_1 \\ \chi_2 \end{bmatrix} \tag{31}$$

A Lyapunov function is defined as follows:

$$V(\chi) = \frac{1}{2} \chi^T P \chi \tag{32}$$

where $\mathbf{P} = \begin{bmatrix} \lambda + 4\varepsilon^2 & -2\varepsilon \\ -2\varepsilon & 1 \end{bmatrix}$.

According to the definition of the adaptive gain Eq. (24), by taking $\beta = 2\varepsilon\alpha$, the time derivative of the Lyapunov function is as follows:

$$\dot{V}(\chi) = -\frac{1}{|s|^{1/2}} \chi^T Q \chi < 0 \tag{33}$$

**Table 1**
Parameters of the stabilization platform.

| Parameters | Value | Unit |
|---|---|---|
| $J_{Ox}$ | 0.00084 | $Kgm^2$ |
| $J_{Oy}$ | 0.001601 | $Kgm^2$ |
| $J_{Oz}$ | 0.001356 | $Kgm^2$ |
| $J_{Ix}$ | 0.000345 | $Kgm^2$ |
| $J_{Iy}$ | 0.001178 | $Kgm^2$ |
| $J_{Iz}$ | 0.001242 | $Kgm^2$ |
| $K_t$ | 0.05 | $Nm/A$ |
| $K_m$ | 0.05 | $Nm/A$ |
| $R$ | 6.4 | $\Omega$ |
| $T_{1,fric}$, $T_{2,fric}$ | 0.0095 | $Nm$ |
| $K_{1f}$, $K_{2f}$ | 2.1 × 10-5 | $Nm/(rad/s)$ |

where $\mathbf{Q} = \begin{bmatrix} 2\lambda\alpha - 2\rho(\lambda + 4\varepsilon^2) & \lambda + 4\varepsilon^2 - 2\varepsilon\rho \\ \lambda + 4\varepsilon^2 - 2\varepsilon\rho & 4\varepsilon \end{bmatrix}$, and $\varepsilon$, $\lambda$ are arbitrary positive constants. The symmetric matrix $\mathbf{Q}$ will be positive definite if $\alpha > \frac{\rho(\lambda + 4\varepsilon^2)}{\lambda} + \frac{(\lambda + 4\varepsilon^2 - 2\varepsilon\rho)^2}{8\lambda\varepsilon}$ [29,13]. Then, it can be concluded that if $\mathbf{Q} > 0$, the time derivative of Eq. (31) $\dot{V}(\chi) < 0$,which implies the stability of the closed loop. The detailed stability analysis is shown in [29,13].

Besides, for practical systems, the control input is always subject to the saturation problem. Considering the realizability in the seeker system, a concisely anti-saturation measure has been taken in the actual implementation. An allowable maximum control input is set for the system, and the absolute value of the actual control input is compared with the set value. If it is greater than or equal to the maximum control input, the control input of the system is set as the maximum control input, which avoids saturation phenomenon.

## 4. Simulation

In order to verify the efficiency of the proposed controller compared with other controllers, numerical simulations have been carried out using the model shown in Section 2.3 in Matlab/ Simulink. The dynamic equations were programmed in S-function. Before the control simulation was added to the system, Eqs. (7), (14), and (17) were used to build the total Simulink model. The parameters of the stabilization platform are listed in Table 1. All the controllers were tested under identical conditions, and both axes were assumed to have the same type of torque motor.

### 4.1. Validation test and coupling effect analysis

The initial condition was set as $[\theta_a, \dot{\theta}_a, \theta_e, \dot{\theta}_e] = [0, 0, 0, 0]$. The roll, pitch, and yaw angular velocities of the base motion as the external disturbance were set as $\omega_{0x} = a_x \sin(2\pi f_x t)$, $\omega_{0y} = a_y \sin(2\pi f_y t)$, $\omega_{0z} = a_z \sin(2\pi f_z t)$. The base angular velocities were as follows: $a_x = a_y = a_z = 1°$, $f_x = f_y = f_z = 3.5Hz$. The numerical simulation results of the coupling effect of the two gimbals with and without the controller are shown in Fig. 4.

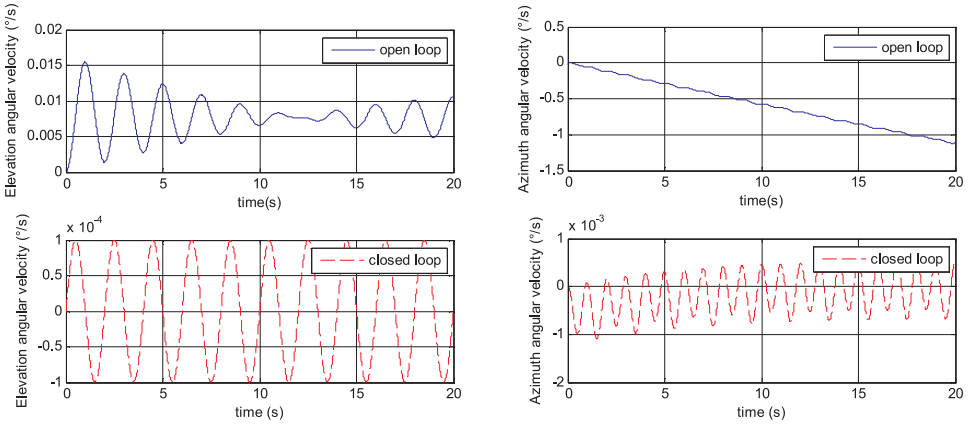


**Fig. 4.** Coupling effect of the base motion on the two gimbals. (a) Coupling effect of elevation axis. (b) Coupling effect of azimuth axis.

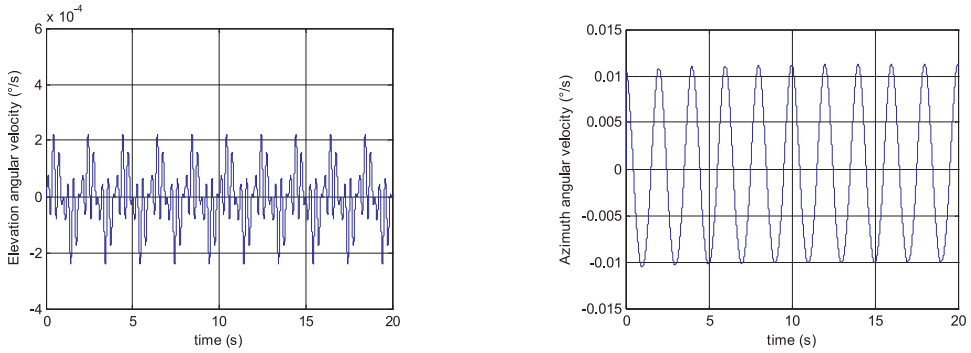


**Fig. 5.** Angular velocities for the elevation and azimuth axes. (a) Coupling output of elevation axis. (b) Coupling output of azimuth axis.

The upper plot of Fig. 4 shows the open loop response of the two gimbals. The lower plot shows the closed loop response of the two gimbals. It can be seen from Fig. 4 that the coupling effect of the base motion on the azimuth axis is larger than coupling effect of the base motion on elevation axis. In addition, in the presence of the controller the coupling effects remain close to zero, while they diverge without the controller.

The cross-couplings between the different channels were also studied. The base angular velocities were taken as follows: $a_x = a_y = a_z = 0°$, $f_x = f_y = f_z = 0Hz$. The elevation angle was set as $\theta_e = 10°$. Firstly, the elevation axis had a sinusoidal input frequency of 3 Hz and amplitude of 1°, and the angular velocity of the azimuth axis was set to 0. Secondly, the azimuth axis input was a sinusoidal signal of 3 Hz frequency and 1° in amplitude, with the angular velocity of the elevation axis set to 0. Here, the system is controlled by a PI controller. The cross-couplings between the different channels are shown in Fig. 5. The elevation axis response is coupled to the azimuth axis' rate, and the coupling effect of the elevation axis is smaller than the coupling effect of the azimuth axis. As a result, the coupling effect cannot not be neglected.

### 4.2. Performance comparison of different controllers

In order to verify the cross-coupling reduction capability of the proposed compound controller, a trapezoidal wave, which is a typical motion status of the seeker, with a maximum at 2°/s was used as the angular velocity reference. Meanwhile, four cases are compared: a conventional PI controller, a PI-DOB controller (which is a traditional controller used in seeker stabilization control), an ASTW controller and the proposed ASTW-ESO controller.

The typical controller of stabilization loop implemented using a PI controller is as follows:

$$G_c(s) = k_p + \frac{k_i}{s} \tag{34}$$

where $k_p$, $k_i$ are the corresponding coefficients of the PI controller. The initial state of the angular velocity and the angular position were set to 0. The controller parameters were tuned through trial and error to make different controllers have the same response time. The control parameters of PI control were $k_{pE} = 2.0$, $k_{iE} = 0.1$ for elevation and $k_{pA} = 2.05$, $k_{iA} = 0.1$ for the azimuth axis, respectively. The same parameters were chosen for the PI-DOB control method. The DOB was chosen as in [14], as follows: the order of the Q filter was 2, the cut-off frequency of the Q filter was 150 Hz, and the nominal model was established using the theoretical mathematical model. The parameters of the ASTW were $\varepsilon_E = 0.9$, $\gamma_1 E = 3$, $\omega_1 E = 50$, $\eta_E = 0.08$, $\mu_E = 0.8$, $\alpha_m E = 0.001$, $\varepsilon_A = 0.9$, $\gamma_1 A = 2$, $\omega_1 A = 260$, $\eta_A = 0.09$, $\mu_A = 0.8$, $\alpha_m A = 0.001$. The same parameters were chosen for the ASTW-ESO. The tuning parameters of the ESO were $w_0$ A= 1500, and $w_0 E = 1500$. The tracking loop adopted a traditional P controller and the proportional parameter was 0.06.

Fig. 6 shows the angular velocity and position tracking responses using various control systems. Based on the results indicated in Fig. 6, it can be noted that the response times of the different controllers were very close to each other. The coupling effect is shown in Fig. 7, while the comparison of the four methods is shown in Table 2. In order to analyze the coupling effect in the simulation, standard deviation is utilized as the error criterion. The standard deviation of the coupling output of the ASTW-ESO controller was 1.9017 × 10-4°/s, which is smaller than the other three controllers. It can be noted that there is considerably reduced coupling effect in the case of ASTW-ESO controller.

### 4.3. Disturbance rejection ability analysis

To verify the robustness of the proposed method, a step response with a disturbance torque was applied to the system. The disturbance rejection ability of the controller is shown in Fig. 8. The results of the comparison are shown in Table 3. In the plot, it is noted that the disturbance susceptibility characteristic of the proposed controller is sharply reduced, and the steady state standard deviation is 0.0009°/s with the proposed controller. The simulation shows that the compound control strategy has excellent of disturbance rejection ability.

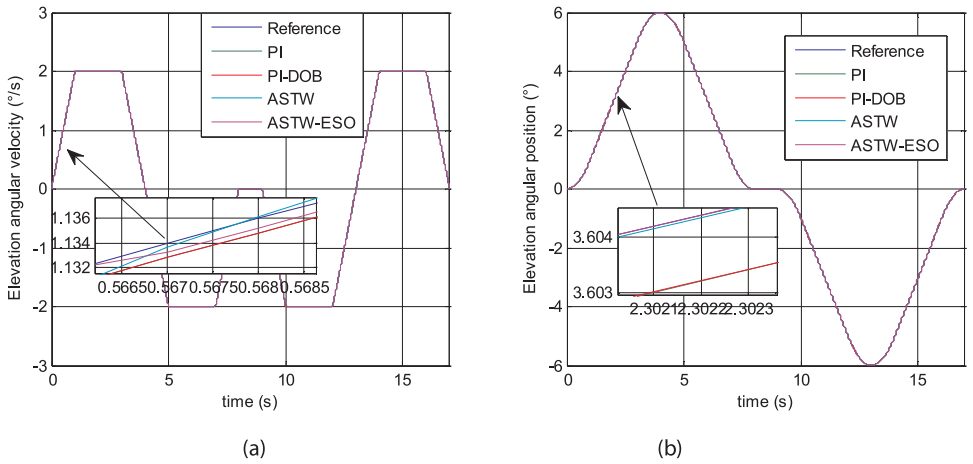


**Fig. 6.** Comparison of elevation axis using various control systems. (a) Angular velocity tracking response. (b) Angular position tracking response.

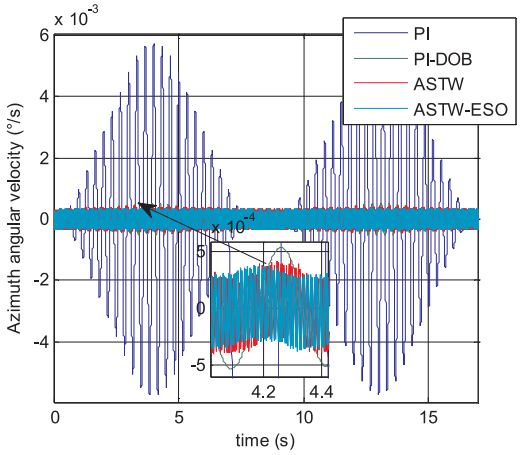


**Fig. 7.** Coupling output of azimuth channel.

**Table 2**
Trapezoidal wave response analysis results of elevation channel.

| Controller | Azimuth channel (Elevation channel move)(°/s) |
|---|---|
| PI | 0.0024 |
| PI-DOB | 2.2407 × 10-4 |
| ASTW | 1.9089 × 10-4 |
| ASTW-ESO | 1.9017 × 10-4 |

## 5. Experiments

To test the proposed controller of the system, experiments were carried out on a five-axis turntable. The experimental setup of the seeker is shown in Fig. 9. The setup mainly includes a five-axis flight simulation turntable, a semi-active laser seeker, the host computer, a seeker driver board, the control board and a laser designator. The five-axis flight simulator consists of a three-axis simulator and a two-axis target simulator. The three-axis simulator can simulate the movement of the missile body in three directions: yaw, pitch and roll. The two-axis turntable can simulate the movement of the target in both yaw and pitch directions. The industrial computer realizes real-time storage of the turntable data and the seeker data through CAN communication. Host computer 1 was used to download programs to the DSP and FPGA and monitor the output of the seeker. Host computer 2 was used to configure the turntable and record its data. The target simulator was mounted on the two-axis turntable, and the laser was derived from a laser designator through optical fiber communication. The controllers were implemented on a DSP, while the laser process algorithm was implemented on a FPGA. All the controllers were discretized using the bilinear transformation. The two controllers are realized on host computer 1 using C language, and then downloaded to the flash of the DSP through the simulator. The other peripheral units, such as power circuit, signal acquisition and processing circuit, and driver circuit were also assembled in the seeker. The control

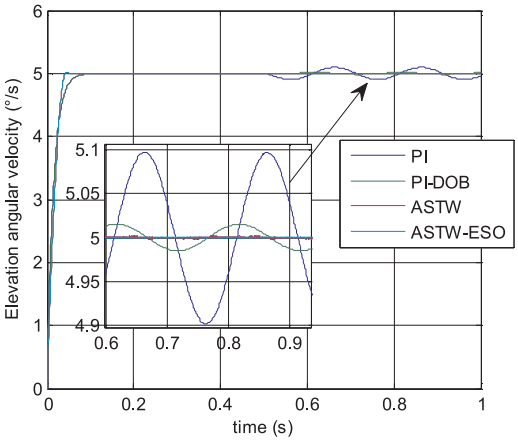


**Fig. 8.** Disturbance rejection ability analysis.

**Table 3**
Step response analysis results of elevation channel.

| Controller | Standard deviation of elevation channel(°/s) |
|---|---|
| PI | 0.0678 |
| PI-DOB | 0.0102 |
| ASTW | 0.0011 |
| ASTW-ESO | 0.0009 |

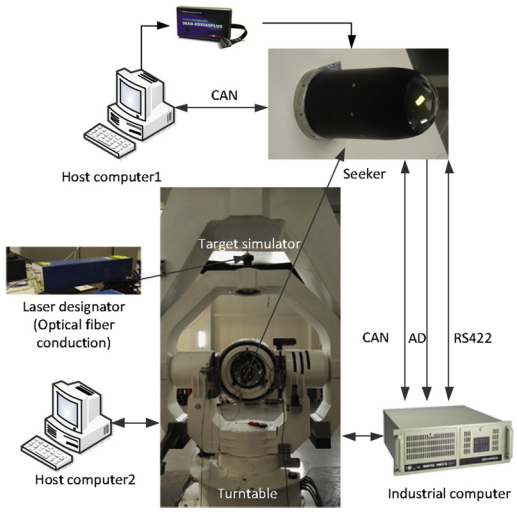


**Fig. 9.** Experimental setup of the seeker.

sampling frequency of the tracking loop was 20 Hz, and that of the stabilizing loop was 1000 Hz. Experiments controller parameters were chosen following the simulation analysis.

### *5.1. Coupling effect experiments*

In order to analyze the coupling effects of the system, the channel coupling coefficient $C$ was utilized:

$$C = \frac{\omega_{spp}}{\omega_{tpp}} \times 100\% \tag{35}$$

where $\omega_{spp}$ is the peak-peak value of the seeker's angular velocity, $\omega_{tpp}$ is the peak-peak value of angular velocity of turntable target.

Two trapezoidal waves were used to verify the effectiveness of the proposed controller. The elevation channel and the azimuth channel are considered in the Section 4.2 and both of them received the same command. In order to demonstrate the effectivity of the

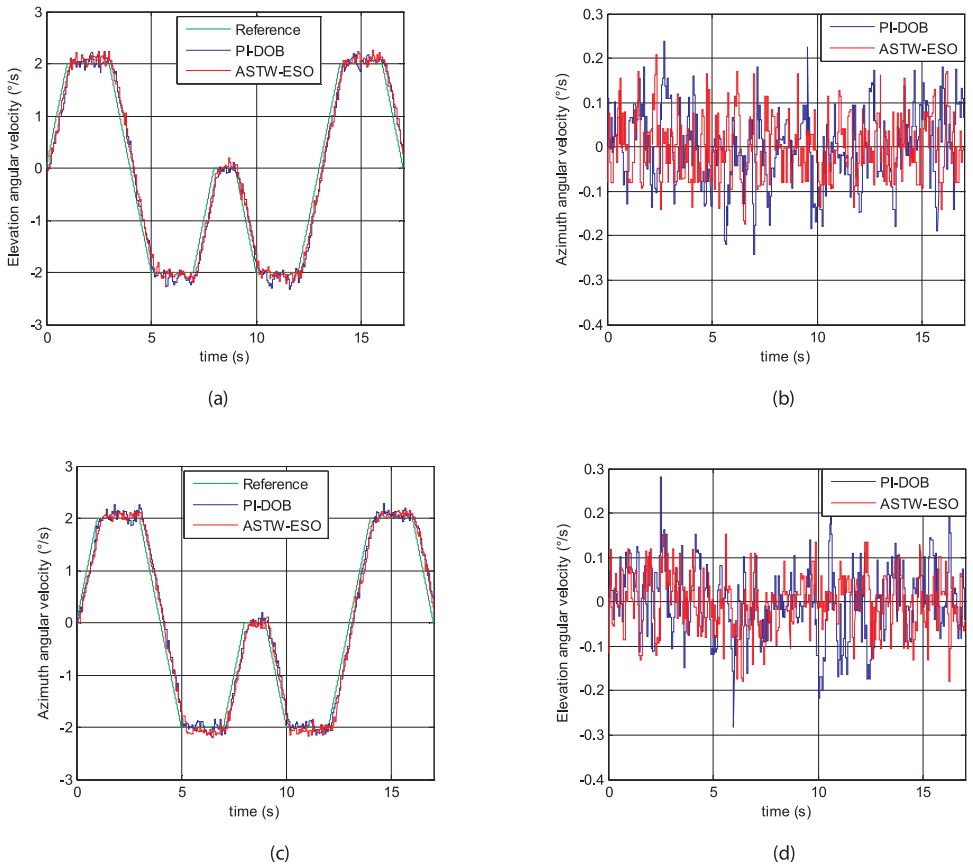


**Fig. 10.** Experiment results of tracking 2°/s trapezoidal wave. (a) Elevation axis response. (b) Azimuth axis coupling response. (c) Azimuth axis response. (d) Elevation axis coupling response.

proposed compound controller, a low angular velocity at 2°/s and a high angular velocity at 6°/s are taken as the command respectively. Fig. 10 shows the results obtained when the seeker tracked a trapezoidal wave of 2°/s with different controllers. Fig. 11 shows the results when the seeker tracked a trapezoidal wave of 6°/s with different controllers.

The results are compared in Tables 4 and 5. The tables summarize the response characteristics of the seeker obtained through different methods. $T_r$ denotes the response time (the time from zero velocity to the maximum angular velocity), *std* is the steady state standard deviation, $C_{AE}$ and $C_{EA}$ are the respective coupling coefficients. As shown in Fig. 10–11 and Table 4–5, both the PI-DOB controller and the ASTW-ESO controller show satisfactory response time, but the ASTW-ESO controller gives a lower steady-state standard deviation and coupling coefficient than PI-DOB. It can be concluded that for the aspect of the cross coupling effect, the compound strategy shows better performance.

### 5.2. Disturbance rejection rate analysis

The system's disturbance rejection ability was tested by tracking a sinusoidal signal. We also tested the disturbance rejection rate in several typical conditions and recorded the results. The disturbance rejection rate $J$ was calculated using the traditional method shown in Eq. (36).

$$J = \frac{|\omega_{out}|}{|\omega_b|} \times 100\% \tag{36}$$

where $\omega_{out}$ is the peak-peak value of angular velocity of the yaw or the pitch axes, and $\omega_b$ is the peak-peak angular velocity value of the three-axis turntable.

We consider the elevation axis as an example, with elevation axis disturbances of amplitude 1° and frequency of 2.5 Hz, and 3° and 0.5 Hz, respectively. $\omega_b$ of the former motion was 7.8540°/s and $\omega_b$ of the latter motion was 4.7127°/s. The target simulator on the two-axis turntable was stationary. Then, the motion data of the elevation gimbal of the platform were acquired and recorded using the industrial computer, i.e. the angular velocity was recorded. The experimental results are shown in Fig. 12 and Table 6. It is seen that the disturbance rejection rate for the two cases is 4.25% and 5.18% with the proposed controller, and 5.19% and 7.42% with the PI-DOB controller, respectively, indicating that the disturbance rejection ability of the proposed ASTW-ESO controller is better than

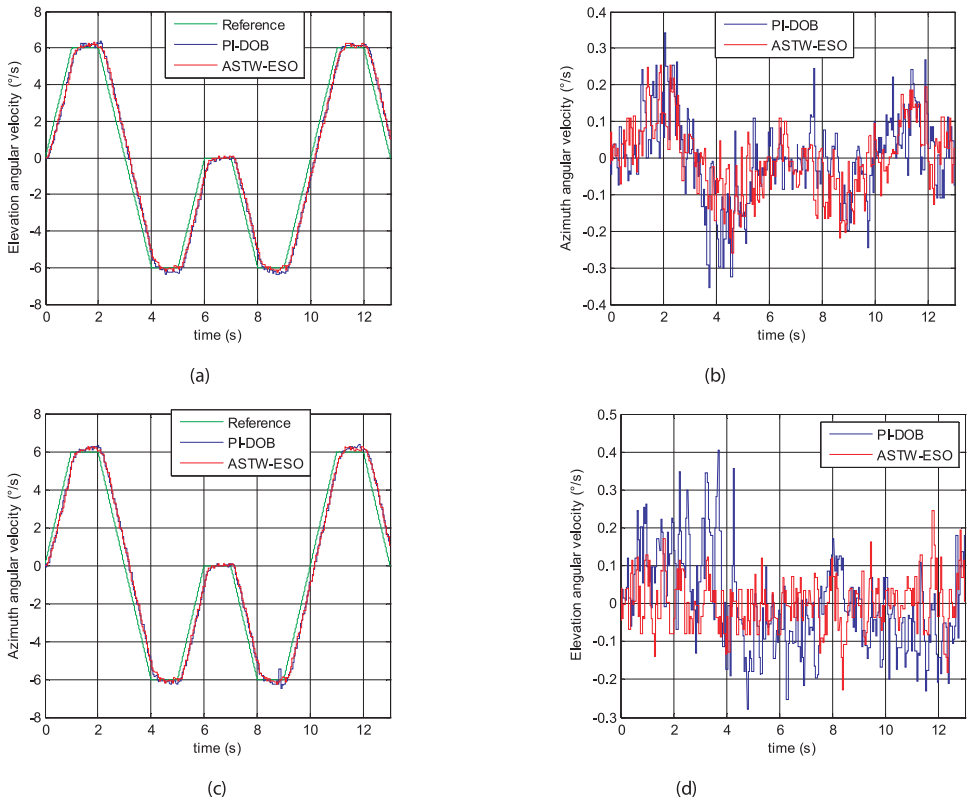


**Fig. 11.** Experiment results of tracking 6°/s trapezoidal wave. (a) Elevation axis response. (b) Azimuth axis coupling response. (c) Azimuth axis response. (d) Elevation axis coupling response.

**Table 4**
trapezoidal wave response of the two channels at 2°/s.

| Signal | 2°/s | | | | | |
|---|---|---|---|---|---|---|
| Motion axis | Elevation | | | Azimuth | | |
| Indexes | $T_r$ | *std* | $C_{EA}$ | $T_r$ | *std* | $C_{AE}$ |
| PI-DOB | 1.141 | 0.0938 | 11.9% | 1.243 | 0.0965 | 14.02% |
| ASTW-ESO | 1.139 | 0.0722 | 9.42% | 1.236 | 0.0564 | 7.66% |

**Table 5**
trapezoidal wave response of the two channels at 6°/s.

| Signal | 6°/s | | | | | |
|---|---|---|---|---|---|---|
| Motion axis | Elevation | | | Azimuth | | |
| Indexes | $T_r$ | *std* | $C_{EA}$ | $T_r$ | *std* | $C_{AE}$ |
| PI-DOB | 1.237 | 0.0799 | 6.77% | 1.271 | 0.117 | 5.73% |
| ASTW-ESO | 1.226 | 0.0762 | 4.08% | 1.263 | 0.0799 | 4.22% |

that of the PI-DOB controller. This verifies the effectiveness of the proposed controller.

The experimental results demonstrate the superior control performance of the proposed control strategy. The static and dynamic performance of the seeker with the proposed controller is better than that of the PI-DOB controller. Using the proposed control strategy, the coupling effect and disturbance rejection rate of the platform improve significantly.

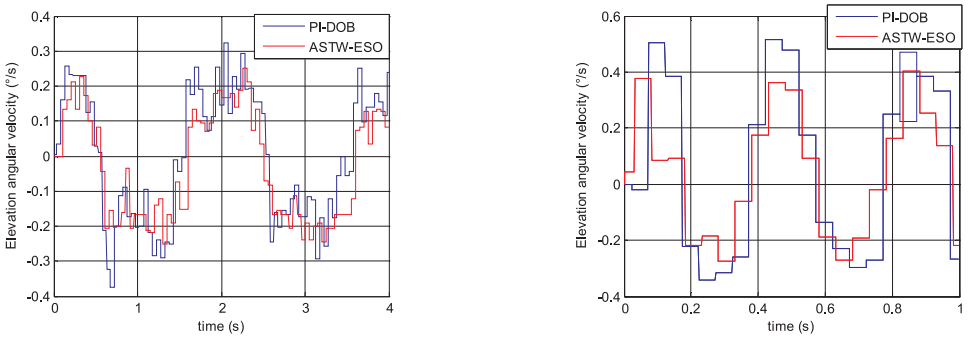


**Fig. 12.** Experimental results of isolation with PI-DOB and ASTW-ESO. (a) Elevation axis response with disturbance of 1°, 2.5 Hz. (b) Elevation axis response with disturbance at 3° and 0.5 Hz.

**Table 6**
Disturbance rejection rate.

| Controller | Disturbance rejection rate | |
|---|---|---|
| | Sin(2.5πt) | 3Sin(0.5πt) |
| PI-DOB | 5.19% | 7.42% |
| ASTW-ESO | 4.26% | 5.18% |

## 6. Conclusions

To achieve high precision of the stabilization platform of the seeker under the external and internal disturbances and system uncertainties, in this paper we propose an ESO-based ASTW sliding mode controller. Three coordinate frames are used to describe the gimbal motion of seeker. Rigid body dynamics and the Newton-Euler equations are used to define the gimbal dynamics considering base angular velocities, cross coupling torque and other non-linear disturbances. Coupling torque and other disturbances are regarded as a total disturbance, which is observed by an ESO and compensated in the system. The ASTW sliding mode controller is used for the stabilizing loop. The Lyapunov principle is used to perform the stability analysis. The merits of the proposed control strategy are validated through implementing simulations and experiments using a trapezoidal wave rate tracking response analysis. The proposed controller is compared with a PI-DOB controller, and the simulation and experiments demonstrate that the proposed control strategy can be very useful in the stabilizing loop of the platform. The results indicate that the proposed controller has not only strong robustness against parameter perturbations and external disturbances, but also against the coupled torque.

## Author contributions

Mingyue Zhang conceived the methodology and wrote the paper. Yongliang Guan designed and performed the experiment. Weiwei Zhao developed the program used in the experiment.

## Conflicts of interest

The authors declare that there is no conflict of interests regarding the publication of this article.

## Acknowledgments

This research is supported by the 3rd Innovation Fund of Changchun Institute of Optics, fine Mechanics and Physics (CIOMP), Chinese Science Academy (CSA) (Grant Number:YYYJ-1122).

## References

[1] X. Zhou, H. Zhang, R. Yu, Decoupling control for two-axis inertially stabilized platform based on an inverse system and internal model control, Mechatronics 24 (December (8)) (2014) 1203–1213.
[2] M.M. Abdo, et al., Stabilization loop of a two axes gimbal system using self-tuning PID type fuzzy controller, ISA Trans. 53 (March (2)) (2014) 591–602.
[3] S. Mondal, S. Sadhu, A. Banerjee, Platform motion disturbances attenuation in a missile seeker subsystem using internal model control, 2013 International Conference on Control, Automation, Robotics and Embedded Systems (CARE), Jabalpur, India, 2013, pp. 1–4.
[4] B. Tamhane, A. Mujumdar, S. Kurode, Mismatched disturbance estimation and compensation for seeker system using higher order sliding mode control, 2014 13th International Workshop on Variable Structure Systems (VSS), Nantes, France, 2014, pp. 1–6.

[5] S. Bendi, N.S.A. Raju, System identification and Robust control for a Stabilization system of a two-axis gimbaled sensor, Ifac Proc. Vol. 47 (December (1)) (2014) 922–927.
[6] J.G. Vadim Utkin, Jingxin Shi, Sliding Mode Control in Electro-mechanical Systems, CRC Press, Taylor and Francis, Boca Raton, London, 2009 Accessed on:.
[7] K. Khalil, Nonliner System, Pearson, 2001 Accessed on: Dec. 28.
[8] S.Y. Chen, S.S. Gong, Hierarchical double integral sliding-mode control for second-order underactuated systems, 2014 CACS International Automatic Control Conference (CACS 2014), Kaohsiung, Taiwan, 2014, pp. 173–178.
[9] Y. Shtessel, M. Taleb, F. Plestan, A novel adaptive-gain supertwisting sliding mode controller: methodology and application, Automatica 48 (May (5)) (2012) 759–769.
[10] A. Levant, Sliding order and sliding accuracy in sliding mode control, Int. J. Control. 58 (November (6)) (1993) 1247–1263.
[11] C. Evangelista, P. Puleston, F. Valenciaga, Wind turbine efficiency optimization. Comparative study of controllers based on second order sliding modes, Int. J. Hydrogen Energy 35 (June (11)) (2010) 5934–5939.
[12] C. VÃazquez, J. Collado, L. Fridman, Super twisting control of a parametrically excited overhead crane, J. Franklin Inst. 351 (April (4)) (2014) 2283–2298.
[13] Y.B. Shtessel, et al., Supertwisting adaptive sliding mode control: a lyapunov design, In Proceedings of the IEEE Conference on Decision and Control CDC 2010, Atlanta, Georgia, USA, 2010, p. 1.
[14] B.K. Kim, K.C. Wan, Advanced disturbance observer design for mechanical positioning systems, IEEE Transactions on Ie. 50 (December (6)) (2003) 1207–1216.
[15] D.K. Kori, J.P. Kolhe, S.E. Talole, Extended state observer based robust control of wing rock motion, Aerosp. Sci. Technol. 33 (January (1)) (2014) 107–117.
[16] J. Han, From PID to active disturbance rejection control, IEEE Trans. Ind. Electron. 56 (February (3)) (2009) 900–906.
[17] J. Yao, Z. Jiao, D. Ma, Adaptive robust control of DC motors with extended state observer, IEEE Trans. Ind. Electron. 61 (July (7)) (2014) 3630–3637.
[18] S. Li, et al., Direct power control of DFIG wind turbine systems based on an intelligent proportional-integral sliding mode control, ISA Trans. 64 (September) (2016) 431–439.
[19] W.H. Chen, et al., Disturbance observer-based control and related methods: an overview, IEEE Trans. Ind. Electron. 63 (February (2)) (2016) 1083–1095.
[20] J KP, L KR, Direct versus indirect line of sight (LOS) stabilization, Ieee Trans. Control. Syst. Technol. 11 (February (1)) (2003) 3–15.
[21] G.G. Rigatos, Adaptive fuzzy control of DC motors using state and output feedback, Electr. Power Syst. Res. (November (79)) (2009) 1579–1592.
[22] B. Yang, et al., Design and real-time implementation of perturbation observer based sliding-mode control for VSC-HVDC systems, Control Eng. Pract. (November (56)) (2016) 13–26.
[23] L. Yi, et al., Active disturbance rejection control based human gait tracking for lower extremity rehabilitation exoskeleton, ISA Trans. (March (67)) (2017) 389–397.
[24] M. Li, et al., Active disturbance rejection control for fractional-order system, ISA Trans. 52 (February (3)) (2013) 365–374.
[25] B.Z. Guo, Z.L. Zhao, On convergence of non-linear extended state observer for multi-input multi-output systems with uncertainty, Control Theory Appl. Iet. 6 (October (15)) (2012) 2375–2386.
[26] A.K. Pati, N.C. Sahoo, Adaptive super-twisting sliding mode control for a three-phase single-stage grid-connected differential boost inverter based photovoltaic system, ISA Trans. (July (69)) (2017) 296–306.
[27] J.A. Moreno, M. Osorio, A Lyapunov approach to second-order sliding mode controllers and observers, 2008 47th IEEE Conference on Decision and Control, Cancun, Mexico, 2008, pp. 9–11.
[28] A. Levant, et al., Homogeneity approach to high-order sliding mode design, Automatica 41 (May (5)) (2005) 823–830.
[29] H. CastaÃ´seda, O.S. Salas-PeÃ´sa, J.D. LeÃ¸sn-Morales, Extended observer based on adaptive second order sliding mode control for a fixed wing UAV, ISA Trans. (January (66)) (2016) 226–232.